EES Batteries

PAPER

View Article Online
View Journal | View Issue

Check for updates

Cite this: *EES Batteries*, 2026, **2**, 623

Mitigating carbothermal reduction in disordered rock-salt cathodes *via* direct electrode-slurry carbon mixing

Gregory Lazaris, † Yixuan Zhang, † Pablo Trevino Lara, Nicolas Brodusch, Raynald Gauvin and Jinhyuk Lee *

Disordered rock-salt (DRX) cathodes have emerged as promising Ni- and Co-free alternatives for lithium-ion batteries, combining the cost advantages of $LiFePO_4$ with the high energy density of layered oxides. Composed of earth-abundant elements such as Mn and Ti, they deliver specific energies above 900 Wh kg^{-1} and capacities over 250 mAh g^{-1}, rivaling or surpassing conventional layered oxides. A critical challenge, however, is their intrinsically low electronic conductivity (10^{-10}–10^{-8} S cm^{-1}), which makes electrochemical performance highly dependent on the type of conductive additives and how they are processed. This need is typically met through mechanical mixing of carbon *via* ball milling, but the consequences of this process on material stability and electrode performance remain insufficiently understood. Using $Li_{1.2}Mn_{0.6}Nb_{0.2}O_2$ as a model DRX system, we reveal that excessive mechanical carbon mixing induces carbothermal reduction (CTR), producing the more soluble Mn^{2+} from Mn^{3+} and converting conductive carbon into insulating lithium carbonate surface species, both of which severely degrade electrochemical performance. These reactions prevent the intended benefits of carbon mixing, leading to increased overpotential, reduced discharge voltage, and accelerated capacity fade. To overcome this challenge, we introduce a direct electrode-slurry mixing method using acid-treated multi-walled carbon nanotubes, which avoids high-energy milling, ensures uniform dispersion, and mitigates CTR-related degradation. This approach enhances cycling stability and voltage retention while remaining compatible with industry-standard slurry processing. Our findings provide mechanistic insights into processing-induced degradation in DRX cathodes and establish a practical pathway toward their scalable, high-performance application in next-generation lithium-ion batteries.

Received 17th December 2025,
Accepted 16th February 2026

DOI: 10.1039/d5eb00236b

rsc.li/EESBatteries

Open Access Article. Published on 16 February 2026. Downloaded on 5/8/2026 1:45:22 AM.
This article is licensed under a Creative Commons Attribution 3.0 Unported Licence.

Broader context

Global electrification needs batteries that are affordable, stable, and composed of abundant elements. Manganese-based disordered rock-salt cathodes promise high specific energy without nickel and cobalt, but their performance is highly sensitive to how conductive carbon additives are introduced during electrode making. This work shows that traditional mechanical carbon mixing can trigger carbothermal reduction; a degradation mechanism that consumes conductive carbon, forms insulating surface species, and reduces manganese to more soluble oxidation states. This results in lower open circuit voltages, increased manganese dissolution, slowed lithium transport, and accelerated capacity fade. To address this, the study replaces carbon ball milling with a direct slurry-mixing method that uses acid-treated carbon nanotubes to build conductive pathways while avoiding carbothermal reduction. This approach raises operating voltage and discharge energy at practical active material loadings and aligns with standard slurry casting methods used in industry. By linking a simple change in mixing protocol to clear gains in stability and energy, the work provides a transferable route to more reproducible production of manganese rich disordered rock salt cathodes for energy storage applications.

Introduction

The global push for renewable energy has significantly increased the demand for advanced lithium-ion battery (LIB) energy storage systems that are both affordable and effective. It is estimated that the global demand for batteries may exceed 5500 GWh by 2040, driven by the expanding electric vehicle market and government initiatives focused on grid-level energy storage for decarbonization.[1,2] Although commercial nickel- and cobalt-based cathodes, such as the layered $LiNi_{0.8}Mn_{0.1}Co_{0.1}O_2$ (NMC811), offer high specific energies (>750 Wh kg^{-1}),[3] the limited abundance and cost of cobalt

Department of Mining and Materials Engineering, McGill University, Montréal, QC H3A 0C5, Canada. E-mail: jinhyuk.lee@mcgill.ca
† These authors contributed equally to this work.

© 2026 The Author(s). Published by the Royal Society of Chemistry

Open Access Article. Published on 16 February 2026. Downloaded on 5/8/2026 1:45:22 AM.
This article is licensed under a Creative Commons Attribution 3.0 Unported Licence.

and the price volatility of nickel has spurred the search for Ni- and Co-free alternatives. Lithium iron phosphate ($LiFePO_4$, LFP) based cathodes, although more affordable, suffer from lower energy densities (~580 Wh kg^{-1}),[4] limiting their use cases in systems requiring highly energy dense LIBs.

A promising Ni- and Co-free alternative is the manganese-based disordered rock-salt cathode (Mn-DRX), which delivers competitive specific energies (>900 Wh kg^{-1})[5] that surpass those of commercial NMC. By replacing expensive Ni and Co with lower-cost transition metals (TMs) like Mn and Ti, Mn-DRX also offers an affordability comparable to LFP.[5] However, a major drawback is its low intrinsic electronic conductivity (10^{-10}–10^{-8} S cm^{-1}), which limits performance unless electrical percolation pathways are extrinsically provided throughout the electrode. This is typically addressed by mechanically mixing Mn-DRX with carbon black (CB, up to ~30 wt%), which partially forms a surface coating while the remainder acts as a conductive additive.[6]

However, recent studies have shown that CB, as the sole conductive additive, has limitations in its ability to form a practical Mn-DRX cathode with high active material (AM) contents (>90 wt% AM, <5 wt% CB).[7] In addition to Mn-DRX's low intrinsic conductivity, the materials are often pulverized into small particles to facilitate Li diffusion, resulting in a high surface area that requires extensive conductive coverage for efficient charge transfer.[8] Yet CB, with its relatively low specific surface area (~45 m^2 g^{-1}) and modest conductivity (10^{-2}–10 S cm^{-1}), is insufficient to fully coat the particle surfaces and support fast charge transport when used at the low contents (<5 wt%) needed for practical AM loadings. Furthermore, the large volume changes that Mn-DRX undergoes during cycling can lead to pore formation and electrode cracking, which further disrupts electrical percolation. The point contacts between CB particles are particularly vulnerable to separation under mechanical stress, resulting in additional conductivity loss.

To address these limitations, multi-walled carbon nanotubes (CNTs) have been explored as an alternative conductive additive.[7] Mechanical mixing of CNTs with Mn-DRX particles has enabled nearly all-AM cathodes with AM contents as high as 96 wt%. CNTs offer significantly higher conductivity (10^3–10^5 S cm^{-1}) and surface area (~250 m^2 g^{-1}) than CB. Their vine-like morphology also facilitates intimate entanglement with Mn-DRX particles, maintaining electrical percolation and enhancing mechanical integrity against cycling-induced cracking, even at low CNT content. Similarly, graphite has been applied to Mn-DRX materials to improve electrode performance under low carbon loading, showing much better results than CB in electrodes containing 10 wt% carbon (80 wt% AM).[9]

While these previous approaches have advanced DRX electrode development, a key limitation remains: they all rely on mechanical ball milling to establish intimate contact between carbon and AM, which is not ideal for scalable electrode fabrication.[10–12] First, ball milling damages the native morphology of Mn-DRX particles, limiting control over microstructure at both particle and electrode levels. Second, it increases processing costs compared with conventional slurry-based methods used in commercial NMC cathode production.[13–15] Most importantly, the mechanical impacts of ball milling generate localized heating and mechanical shear stress that promote side reactions between Mn-DRX and carbon, degrading cell performance. Yet these side reactions remain insufficiently understood, leaving Mn-DRX electrode design highly dependent on trial-and-error optimization of milling conditions.

Herein, we systematically investigate the impact of mechanical carbon mixing on $Li_{1.2}Mn_{0.6}Nb_{0.2}O_2$ (LMNO) as a representative Mn-DRX compound. Our structural and electrochemical analyses demonstrate that while intensified mixing enhances carbon-DRX contact and homogenizes carbon distribution, it simultaneously induces carbothermal reduction (CTR) as the principal side reaction. This process irreversibly degrades the material, such as by reducing Mn^{3+} to the more soluble Mn^{2+}, thereby accelerating Mn dissolution, and by consuming conductive carbon to form insulating lithium impurity phases on the surface, both of which impede charge-transfer kinetics and accelerate cycling degradation.[16] Thus, although mechanical carbon mixing is intended to enhance conductivity and facilitate redox kinetics, the occurrence of CTR can prevent these benefits unless carefully controlled, and can instead increase overpotential, lower the average operating potential, and accelerate both voltage decay and capacity fade. To address these challenges, we propose a direct electrode-slurry (DS) carbon mixing method using acid-treated functionalized CNTs (ATCNTs) as the conductive additive. By uniformly distributing conductive carbon in the electrode while avoiding mechanical carbon mixing, CTR-related degradation is mitigated, preserving Mn-DRX particles and preventing conductive carbon from transforming into insulating surface carbonate species. These improvements, in turn, enhance capacity and voltage retention while simplifying electrode fabrication in alignment with industrial practices. Our findings provide mechanistic insights and a practical pathway toward scalable, high-performance Mn-DRX cathodes.

Results and discussion

Impact of mechanical carbon mixing on LMNO crystal and microstructure

$Li_{1.2}Mn_{0.6}Nb_{0.2}O_2$ (LMNO) was selected as a representative Mn-DRX cathode, given its extensive investigation in the literature. The material was synthesized *via* a solid-state method (as-synthesized, AS-LMNO) and subsequently pulverized by ball milling (as-pulverized, AP-LMNO). For electrode preparation and characterization, AP-LMNO was further ball milled with CB to achieve mechanical carbon mixing/coating. In this study, AP-LMNO and CB were combined in a 70 : 20 weight ratio to reflect the typical AM : CB ratio used in Mn-DRX electrodes in the literature, which are commonly formulated as 70 AM : 20 CB : 10 binder (PTFE or PVDF).

© 2026 The Author(s). Published by the Royal Society of Chemistry

Open Access Article. Published on 16 February 2026. Downloaded on 5/8/2026 1:45:22 AM.
This article is licensed under a Creative Commons Attribution 3.0 Unported Licence.

Fig. 1a presents the X-ray diffraction (XRD) patterns of AS-LMNO and AP-LMNO, confirming the formation of the DRX phase. Ball milling of AS-LMNO results in significant peak broadening due to reduced crystallinity, consistent with previous reports.[17] A shift toward lower angles is also observed, corresponding to an increase in lattice parameter from ~4.17747 Å to ~4.19037 Å, as determined by XRD refinement (Fig. S1a and b). While peak broadening has been widely discussed in the literature, the subtle lattice expansion is often overlooked and is likely attributed to self-reduction of LMNO during particle pulverization in an argon-filled jar. SEM images of AS-LMNO and AP-LMNO can be found in the SI (Fig. S2).

Following the initial pulverization of LMNO, AP-LMNO was further mixed with CB in a 70 : 20 weight ratio under various conditions using a planetary ball mill. The CB-LMNO samples are labelled according to rotation speed per minute (RPM) and milling duration (*e.g.*, 300-1: 300 rpm for 1 hour). Fig. 1b and c show scanning electron microscopy (SEM) and transmission electron microscopy (TEM) images of 300-1 and 600-1 CB mixed LMNO, respectively. For the 300-1 and 600-1 SEM images, energy-dispersive spectroscopy (EDS) elemental maps are overlaid to distinguish CB (shown in red) from the LMNO particles. In the EDS maps, Mn is shown in cyan, O in green, and Nb in magenta, and their combination represents the LMNO phase. Full EDS maps can be found in the SI (Fig. S3).

SEM-EDS maps show that increasing the mixing speed from 300 to 600 rpm leads to a more uniform distribution of CB, as indicated by the more homogeneous dispersion of red-coded particles. The spherical morphology of CB observed in the 300-1 sample becomes less distinct in the 600-1 sample, suggesting particle deformation at higher RPMs and a possible transition from CB-LMNO point contacts to planar contacts. This can be seen more clearly in the TEM images, where the spherical CB morphology (blue boxes in Fig. 1b) in the 300-1 sample is seen less in the 600-1 sample (red boxes in Fig. 1c) indicating improved carbon coverage and planar contact. Additionally, LMNO particles in both 300-1 and 600-1 appear smaller than those in AP-LMNO (Fig. S2b). These microstructural changes may enhance charge transfer in LMNO, assuming other factors remain identical.

XRD analysis of the CB mixed LMNO reveals that the RPM during CB mixing also influences the LMNO crystal structure. Fig. 1d and e present the (111), (002), and (022) peaks for the 300-1, 400-1, 500-1, 600-1, and 600-5 samples, along with their

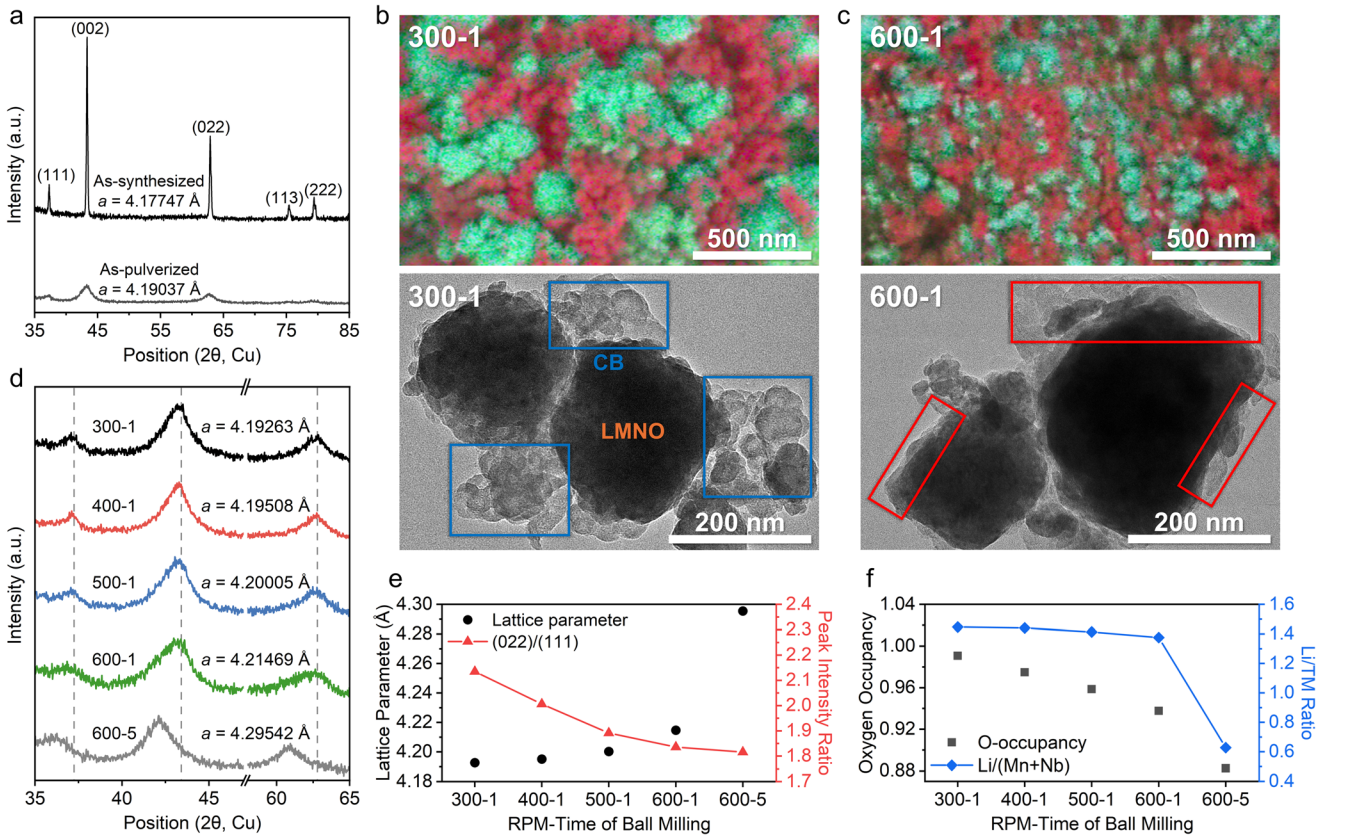

Fig. 1 Structural characterization of as-synthesized (AS) and as-pulverized (AP) $Li_{1.2}Mn_{0.6}Nb_{0.2}O_2$ (LMNO) and CB mixed LMNO powders prepared under different mixing conditions (300/400/500/600 rpm for 1 hour; and 600 rpm for 5 hours). (a) X-ray diffraction (XRD) patterns of AS and AP-LMNO. SEM and TEM images of (b) 300-1 and (c) 600-1 CB mixed LMNO. EDS maps are overlaid on the SEM images. (d) XRD patterns of CB mixed LMNO and their corresponding *a*-lattice parameters with increasing mixing conditions (RPM-time) determined by Rietveld refinement. (e) Rietveld refinement determined *a*-lattice parameter and (022)/(111) peak ratio of CB mixed LMNO. (f) Rietveld refinement determined oxygen occupancy and Li/(Mn + Nb) ratio of CB mixed LMNO.

© 2026 The Author(s). Published by the Royal Society of Chemistry

Open Access Article. Published on 16 February 2026. Downloaded on 5/8/2026 1:45:22 AM.
This article is licensed under a Creative Commons Attribution 3.0 Unported Licence.

refined lattice parameters and (022)/(111) peak intensity ratios (see Fig. S1c–g for refinement details). With increasing RPM and milling duration, peak broadening becomes more pronounced, particularly for the 600-1 and 600-5 samples relative to 300-1. This broadening likely reflects increased pulverization of AP-LMNO during CB mixing, consistent with SEM observations (Fig. 1b, c and Fig. S4). Peak positions also shift systematically to lower angles, indicating an increase in lattice parameter, from ~4.19263 Å (300-1) to ~4.21469 Å (600-1) and ~4.29542 Å (600-5). The intensified milling conditions also lead to a decreased (022)/(111) peak intensity ratio.

These changes are consistent with partial Mn reduction (Mn^{2+} formation) and oxygen loss induced by CTR. The lattice expansion observed from XRD refinement (Fig. 1e) can be attributed to the reduction of Mn^{3+} to the larger Mn^{2+} cation, together with the introduction of oxygen vacancies, which reduces electrostatic screening and enhances cation–cation repulsion. The decreased (022)/(111) peak intensity ratio can be rationalized by two models (Fig. 1f), both requiring oxygen loss: (i) the oxygen-vacancy (OV) model, where oxygen vacancies form in the lattice, and (ii) the cation-densification (CD) model, where TMs at the particle surface back-diffuse into the bulk after oxygen loss, thereby increasing the TM content and decreasing the Li/TM ratio. Although XRD refinements cannot decisively distinguish between these scenarios, both indicate oxygen loss and Mn reduction for charge compensation. The increasing oxygen vacancy concentration (OV model) or the decreasing Li/TM ratio (CD model) with stronger CB mixing both demonstrate that aggressive mechanical carbon milling triggers CTR-induced oxygen loss in LMNO.

We performed X-ray photoelectron spectroscopy (XPS) on the CB-LMNO samples (300-1, 400-1, 500-1, 600-1, and 600-5) to investigate the effect of CB mixing on the electronic structure of LMNO and the formation of surface species. As shown in Fig. 2a, the O 1s spectra exhibit a main peak at ~530.6 eV, corresponding to lattice oxygen (O^{2-}) in LMNO. The peaks at ~531.5 eV and ~532.5 eV are attributed to surface lithium/oxygen species (ROLi) and carbonate species (CO_3^{2-}) respectively.[18–21] ROLi includes various species of lithium oxide and lithium alkoxides.[21] The peak at ~533.8 eV is assigned to other oxygen species such as C–O or oligomeric O═C–O.[19,21] The peak at ~534.8 eV is assigned to weakly bound H_2O, likely from residual surface moisture.[22–24] As CB mixing intensifies from 300-1 to 600-5, the relative intensity of the ~532.5 eV carbonate peak systematically increases compared to the lattice oxygen peak.

The C 1s spectra in Fig. 2b further support this carbonate formation, showing progressive oxidation of carbon, with CB as the original carbon source. The main peak at ~284.8 eV corresponds to C–C/C–H bonds from non-oxidized carbon, while peaks at ~286 eV (C–OH/C–O–C), ~287.2 eV (C═O), ~288.6 eV (O═C–O), and ~290.5 eV (CO_3^{2-}) represent oxygenated carbon species.[18,25] As CB mixing intensifies, the relative intensity of oxygenated species increases compared to the non-oxidized carbon peak, indicating progressive oxidation of CB during the mixing process to form carbonate species. Finally, Li 1s XPS data (Fig. 2c) shows a progressive decrease in the intensity of the lattice Li peak (~54.8 eV) and an increase in the higher energy peak linked to Li surface species (~55.5 eV, Li_2CO_3/$LiHCO_3$).[20,26,27] Together with the ROLi and carbonate

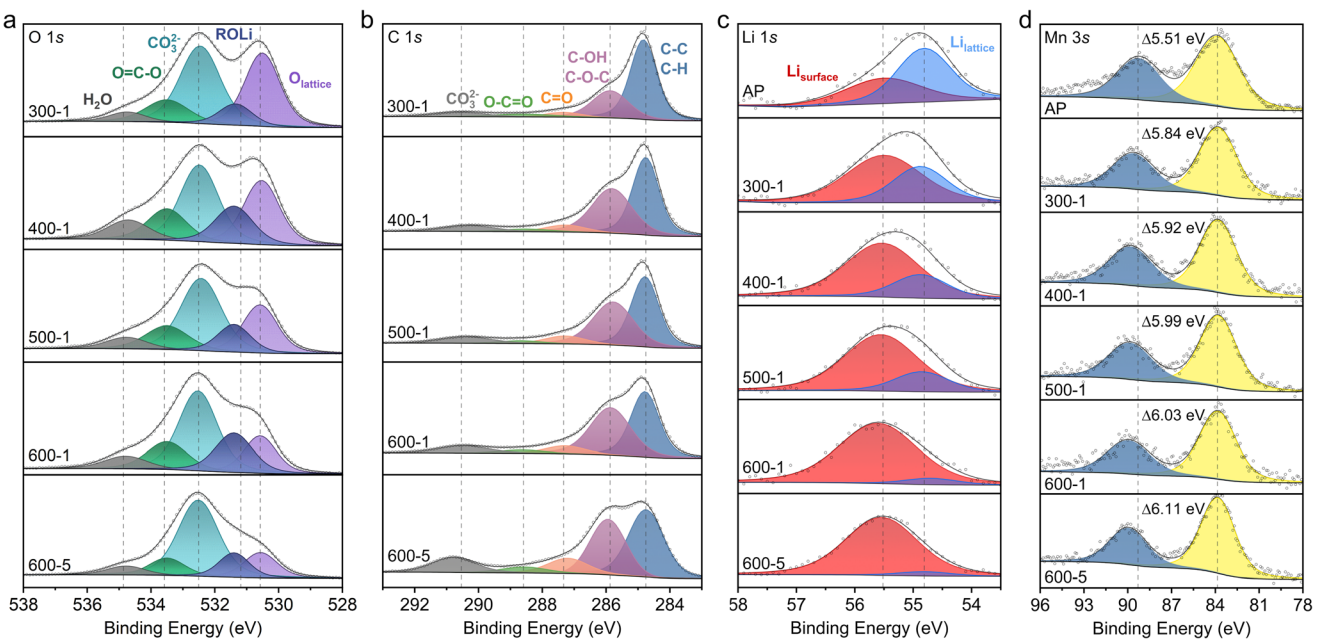

Fig. 2 X-ray photoelectron spectroscopy (XPS) of CB mixed LMNO powders prepared under different mixing conditions (300/400/500/600 rpm for 1 hour; and 600 rpm for 5 hours). (a) O 1s, (b) C 1s, (c) Li 1s and (d) Mn 3s XPS spectra charge corrected to C 1s C–C/C–H at 284.8 eV of the CB mixed LMNO powders. AP-LMNO is included for Li 1s and Mn 3s.

© 2026 The Author(s). Published by the Royal Society of Chemistry

Open Access Article. Published on 16 February 2026. Downloaded on 5/8/2026 1:45:22 AM. This article is licensed under a Creative Commons Attribution 3.0 Unported Licence.

signatures in O 1s, these trends indicate growth of Li-containing surface phases generated by CTR during intense carbon milling.

Because CB mixing was conducted in sealed argon-filled ball mill jars, the oxygen required for carbon oxidation must originate from the LMNO particles, leading to the reduction of TMs in LMNO. Consistently, the Mn 3s XPS spectra in Fig. 2d exhibit a shift indicative of Mn reduction, supporting this mechanism. The Mn 3s spectrum shows spin-energy splitting between two peaks, where a larger separation corresponds to a more reduced Mn oxidation state.[28–30] As a reference, the reported peak separations for MnO (Mn^{2+}), Mn_2O_3 (Mn^{3+}), and MnO_2 (Mn^{4+}) fall within 5.5–6.1 eV, 5.2–5.6 eV, and 4.1–4.7 eV, respectively.[31–35] This was confirmed further by performing XPS on these compounds (Fig. S5a), and seeing a similar trend in peak separations. With intensified CB mixing, the Mn 3s peak separation increases from 5.51 eV for the AP-LMNO sample to 5.84 eV for 300-1 and up to 6.11 eV for the 600-5 sample, indicating a significant increase in Mn^{2+} content and thus Mn reduction. Although the surface-sensitive nature of XPS limits quantitative assessment of bulk Mn reduction, these results clearly demonstrate carbon oxidation occurring alongside Mn reduction, resembling a CTR process despite the absence of an external heat source. Meanwhile, the Nb 3d XPS spectra show no significant change (Fig. S5b), indicating that the Nb oxidation state remains unaffected. Taken together, the observations from our CB-LMNO mixing experiments can be rationalized by a CTR reaction similar to the following:

$$\mathrm{Li_{1.2}Mn_{0.6}Nb_{0.2}O_2}\left(\mathrm{Mn^{3+}}\right) + x\mathrm{C} \rightarrow \mathrm{Li_{1.2-2}}_{x}\mathrm{Mn_{0.6}Nb_{0.2}O_{2-3}}_{x}\left(\mathrm{Mn^{<3+}}\right) + x\mathrm{Li_2CO_3} \quad (1)$$

Here, the maximum amount of carbon (x) participating in the reaction would be governed by (i) the total carbon content relative to LMNO. Additionally, (ii) a larger interfacial contact area between carbon and LMNO particles and (iii) localized temperature rise from the dissipation of mechanical energy, together with mechanical shear-induced lattice distortion during ball milling, can kinetically promote the CTR process, even in the absence of externally applied heating. As a result, a higher degree of CTR is expected with more vigorous carbon mixing, which converts conductive carbon into insulating surface carbonate species and partially reduces Mn in LMNO, undermining the original goal of enhancing electrode conductivity. Here, we leave the detailed atomistic understanding of this CTR process to future studies, including efforts to decouple the respective roles of localized thermal effects and mechanical shear stress during ball milling.

Importantly, we note that the same CTR-induced degradation is also observed for the direct one-step carbon mixing of as-synthesized LMNO particles, in which particle pulverization and carbon incorporation occur simultaneously. This method likewise leads to Mn reduction and surface carbonate formation, demonstrating that CTR is intrinsic to mechanically driven carbon mixing processes rather than specific to the use of pre-pulverized DRX particles (Fig. S6 and S7).

Effects of CTR on electrochemical performance of LMNO

We conducted electrochemical tests using Li||LMNO half-cells (70 : 20 : 10, LMNO : CB : PTFE, 1.5–4.8 V, 40 mA g^{-1}, 25 °C) to investigate the effect of varying degrees of carbon mixing on LMNO performance. To preserve the original state of the CB–LMNO mixtures, dry-processed cathode films were prepared inside an argon-filled glovebox, avoiding air exposure. Wet-processed electrode performance, which is more relevant for industrial applications and directly related to the slurry process, will be discussed later.

First-cycle voltage profiles and corresponding dQ/dV plots (Fig. 3a and b) highlight the impact of intensified carbon mixing on electrochemical behavior. With stronger mixing, samples exhibit progressively lower open-circuit voltages (OCVs) during the resting stage before the first charge, marked by dashed lines in Fig. 3a. The OCVs for 300-1 and 400-1 remain nearly identical at 2.470 and 2.472 V, whereas more pronounced decreases are observed for 500-1, 600-1, and 600-5, with values of 2.326, 2.143, and 2.068 V, respectively (Fig. 3a). This systematic OCV reduction prior to cycling reflects increased Mn reduction at the electrode surface caused by CTR, consistent with the XPS results discussed earlier.

Although carbon mixing is generally expected to enhance electrode conductivity and reversible capacity, our results show a significant decline in capacity with intensified mechanical mixing due to CTR. The first discharge capacity drops from 303 mAh g^{-1} for 300-1 to 288, 267, 242, and 118 mAh g^{-1} for 400-1, 500-1, 600-1, and 600-5, respectively. Intensified carbon mixing also progressively suppresses the high-voltage plateau at 4.2–4.3 V in the voltage profile, typically attributed to oxygen oxidation (Fig. 3a), and eliminates the corresponding charging dQ/dV peak near 4.3 V (Fig. 3b).[36] Additionally, the discharging dQ/dV peak at ~3.0–3.3 V, generally associated with Mn reduction, shifts to lower voltages as milling intensity increases (Fig. 3b). This shift likely reflects an increased contribution from lower-voltage Mn^{3+}/Mn^{2+} reduction over Mn^{4+}/Mn^{3+} reduction after enhanced CTR. Overall, these results indicate that LMNO is progressively reduced with intensified carbon mixing, shifting the redox mechanism from Mn^{3+}/Mn^{4+} and oxygen redox to $Mn^{2+}/Mn^{3+}/Mn^{4+}$ and a diminished oxygen redox process. Consequently, both OCV and average discharge voltage decrease significantly with intensified CB mixing over 50 cycles (Fig. 3c).

In addition to changes in operating potential and redox mechanisms, intensified carbon mixing and the resulting CTR also affect Li transport kinetics. Fig. 3d compares the apparent Li diffusivities (D_{Li}) of CB mixed LMNO samples during the first charge, as determined by galvanostatic intermittent titration technique (GITT) measurements (Fig. S8). Under intense CB mixing conditions, the apparent Li diffusivity consistently decreases: the 300-1 sample shows the highest diffusivity (generally between ~1×10^{-16} and 3×10^{-15} cm^2 s^{-1}), while the 600-5 sample exhibits a markedly lower value (largely between ~1×10^{-17} and 3×10^{-16} cm^2 s^{-1}). This reduction is likely linked to CTR-induced metal densification at the particle

© 2026 The Author(s). Published by the Royal Society of Chemistry

Open Access Article. Published on 16 February 2026. Downloaded on 5/8/2026 1:45:22 AM.
This article is licensed under a Creative Commons Attribution 3.0 Unported Licence.

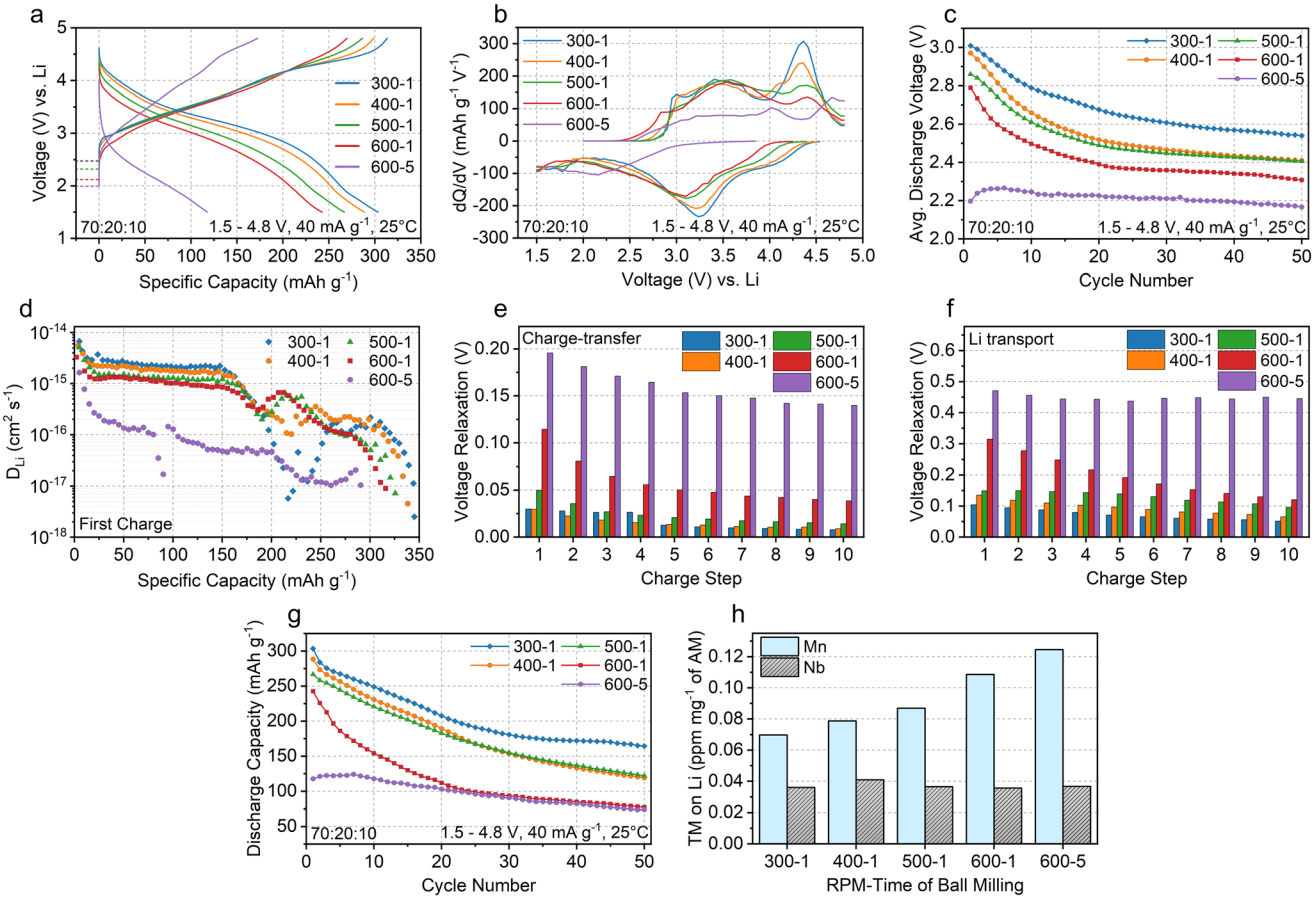

Fig. 3 Electrochemical performance of CB mixed LMNO prepared under different mixing conditions (300/400/500/600 rpm for 1 hour; and 600 rpm for 5 hours). (a) 1st-Cycle voltage profiles of CB mixed LMNO cycled at 40 mA g^{-1} between 1.5–4.8 V. The OCV during the resting stage before the first charge is labelled with a dashed line at the start of charging. (b) d*Q*/d*V* plot of 1st-cycle CB mixed LMNO. (c) Average discharge voltage of CB mixed LMNO over 50 cycles. (d) The estimated Li diffusivity from galvanostatic intermittent titration technique (GITT) measurements during charging. (e and f) Voltage relaxations obtained from GITT data of the first 10 charging steps. (g) Capacity retention of CB mixed LMNO over 50 cycles. (h) Concentration of Mn and Nb detected on Li-metal anode after 50 cycles determined from inductively coupled plasma optical emission spectroscopy (ICP-OES).

surface. By increasing the TM content and reducing the Li/TM ratio, this cation-densified surface layer hinders Li transport by lowering the fraction of diffusion-permissive 0-TM channels, which are known to enable fast Li diffusion in DRX materials.[37,38]

Interestingly, at charge states of ~180–260 mAh g^{-1}, the 300-1 sample shows lower diffusivity than the 400-1, 500-1, and 600-1 samples. This trend likely arises because the minimal CTR in 300-1 leads to more extensive O-oxidation in this window. In turn, Li diffusion becomes coupled with local structural rearrangements such as oxygen dimer formation and TM migration, which are intrinsically slower than the TM oxidation processes dominant in more CTR-affected samples, where structural reorganization is less pronounced.

A closer examination of the voltage relaxation in our GITT results reveals that intensified carbon mixing degrades charge transfer kinetics and other non-diffusion-controlled processes, in addition to affecting Li transport. The relaxation behavior consists of two components: (i) an initial, rapid voltage drop (Fig. 3e and Fig. S8a) associated with IR drop and charge-transfer (CT) resistance at the electrode/electrolyte interface, and (ii) a slower, time-dependent relaxation (Fig. 3f and Fig. S8a) governed by mass transport resistance, including Li diffusion within the DRX particles and ionic transport through the electrolyte-filled pores in the cathode. Fig. 3e and f highlight the first 10 charging steps, each corresponding to a charge of 5 mAh g^{-1}. Both relaxation components systematically increase with intensified milling and CTR. In particular, the initial rapid voltage drop, which primarily arises from IR and CT resistances, is minimal in the 300-1 sample (below 0.05 V across all steps), increases to nearly 0.1 V in the 600-1 sample, and further doubles to approximately 0.2 V in the 600-5 sample. This trend signifies a substantial rise in interfacial impedance and CT resistance following intensified carbon mixing, which promotes CTR and results in the formation of insulating carbonate species rather than enhancing electrical conductivity.

Fig. 3g presents the discharge capacities of LMNO samples with varying degrees of carbon mixing over 50 cycles. Samples

© 2026 The Author(s). Published by the Royal Society of Chemistry

Open Access Article. Published on 16 February 2026. Downloaded on 5/8/2026 1:45:22 AM. This article is licensed under a Creative Commons Attribution 3.0 Unported Licence.

subjected to more intensive carbon mixing exhibit overall lower capacities. The 300-1 sample clearly maintains the highest absolute capacities throughout cycling. It also shows better percentage retention (~54.2%) than the 400-1 (~41.3%), 500-1 (~45.7%), and 600-1 (~31.9%) samples. Although the 600-5 sample shows a higher percentage retention (~63.0%), this is largely due to its much lower initial capacity, which reduces the denominator in the capacity retention calculation.

Overall, it is noteworthy that, although more intensive CB mixing is expected to produce a more uniform carbon distribution and thus a more robust electronic percolation network, the electrochemical performance is degraded rather than improved. In the present electrodes, the high carbon loading (20 wt% CB) already ensures electrode-level electronic percolation, even in the presence of local carbon heterogeneity. Under these conditions, CTR-induced damage to the DRX particles becomes the dominant factor governing performance degradation, outweighing the benefit of improved carbon homogeneity.

We find that the accelerated capacity fading associated with strong CB mixing accompanies increased Mn dissolution. Fig. 3h shows the amounts of Mn and Nb (in ppm mg^{-1} of AM, LMNO) detected on the Li chip collected from Li||LMNO half-cells after 50 cycles. The amount of Mn deposited on the Li chip systematically increases with the intensity of CB ball milling. This trend is likely due to a higher fraction of Mn^{2+} at the LMNO particle surface under aggravated CTR conditions, as Mn^{2+} is known to dissolve more readily into the electrolyte than Mn^{3+} or Mn^{4+}.[39,40] Moreover, the additional, albeit modest, reduction in LMNO particle size upon CB mixing (Fig. S4) can increase the surface area exposed to the electrolyte and may therefore contribute to Mn dissolution, alongside Mn^{2+} formation induced by the CTR process. The resulting Mn dissolution depletes redox-active species in the cathode and destabilizes the Li-metal anode by degrading the solid–electrolyte interphase layer, thereby accelerating capacity fade in the Li||LMNO half-cells.

In contrast, the amount of Nb detected on the Li chip remains largely unchanged across the mechanically carbon mixed samples. This behavior is consistent with the fact that CTR preferentially reduces Mn^{3+} to Mn^{2+}, whereas Nb remains in the Nb^{5+} oxidation state and is therefore not directly affected by redox processes. Consequently, in the absence of a change in oxidation state, the intrinsic solubility of Nb in the electrolyte is expected to remain similar. Nevertheless, oxygen loss and the associated surface disorder induced by CTR can generate under-coordinated Nb^{5+} environments at the DRX particle surface, which weaken Nb–O bonding and can indirectly facilitate Nb dissolution without involving Nb redox. As will be shown later in this work, eliminating the mechanical carbon mixing step markedly suppresses both Nb and Mn dissolution.

Direct slurry carbon mixing of LMNO with acid-treated multi-wall carbon nanotubes

Given the detrimental electrochemical impacts associated with mechanical CB mixing and CTR, we propose a direct electrode-slurry (DS) carbon mixing approach that eliminates the carbon ball-milling step entirely. Unlike traditional cathode chemistries such as layered oxides, which are routinely prepared by single-step slurry casting of AM, carbon additive, and binder, DRX cathodes require mechanical pulverization followed by separate carbon milling to achieve adequate dispersion and conductivity. However, as previously discussed, this carbon milling process inadvertently induces CTR, significantly degrading cathode performance. Attempts to directly incorporate carbon additives (CB or CNTs) into DRX slurries without mechanical milling typically result in poor dispersion and electrical conductivity, an issue explored further in subsequent sections.

Recent reports suggest that multi-walled CNTs (hereafter referred to as CNTs), provide superior performance relative to CB due to their unique vine-like morphology, high conductivity, and higher surface area coverage.[7] Thus, CNTs were the primary carbon additive investigated in this portion of our study. To overcome the dispersion challenges encountered with pristine CNTs, we applied a straightforward oxidative acid treatment method to functionalize and detangle CNT bundles (termed acid-treated CNTs, ATCNTs). This functionalization significantly improves CNT dispersibility in polar solvents critical for slurry casting, particularly *N*-methylpyrrolidone (NMP).

XPS and Raman spectroscopy were utilized to confirm successful oxygen functionalization and structural modification of CNT surfaces. Fig. 4a shows the comparative O 1s XPS spectra for pristine CNTs and ATCNTs. The spectra reveal oxygen-functionalization-related peaks in ATCNTs, corresponding to C═O/C–OH at ~532 eV and COOH/C–O at ~533.2 eV, expected for our acid treatment process.[41–43] In contrast, pristine CNTs exhibited almost no O 1s signal. Results from the C 1s spectra (Fig. 4b) further confirm enhanced oxygen functionalization, with intensified peaks related to C–O, C═O, and O–C═O groups compared to pristine CNTs.[42–44] Raman spectroscopy (Fig. 4c) further supports these findings, demonstrating an increased intensity ratio between the D-band and G-band (I_D/I_G), which rises from 0.86 for pristine CNTs to 1.01 for ATCNTs. This result aligns with increased surface defects and functionalization following acid treatment.[45,46]

Dispersion quality was visually assessed by suspending 1 wt% CNTs/ATCNTs in NMP through bath sonication. The ATCNT suspension remained stable over 24 hours, whereas the pristine CNTs were unable to disperse even during the sonication (Fig. 4d). SEM imaging in Fig. 4e also confirms the detangling effect of acid treatment, revealing loosely arranged ATCNTs compared to the more densely entangled pristine CNTs which form a dense rope-like structure. Such morphological modifications enhance the effective surface area and improve contact between the CNTs and LMNO particles, improving electrical conductivity and electrochemical performance.

To quantitatively assess carbon dispersion and percolation in electrodes prepared *via* the DS process, pristine electrodes were analyzed through cross-sectional SEM imaging combined

Open Access Article. Published on 16 February 2026. Downloaded on 5/8/2026 1:45:22 AM.
This article is licensed under a Creative Commons Attribution 3.0 Unported Licence.

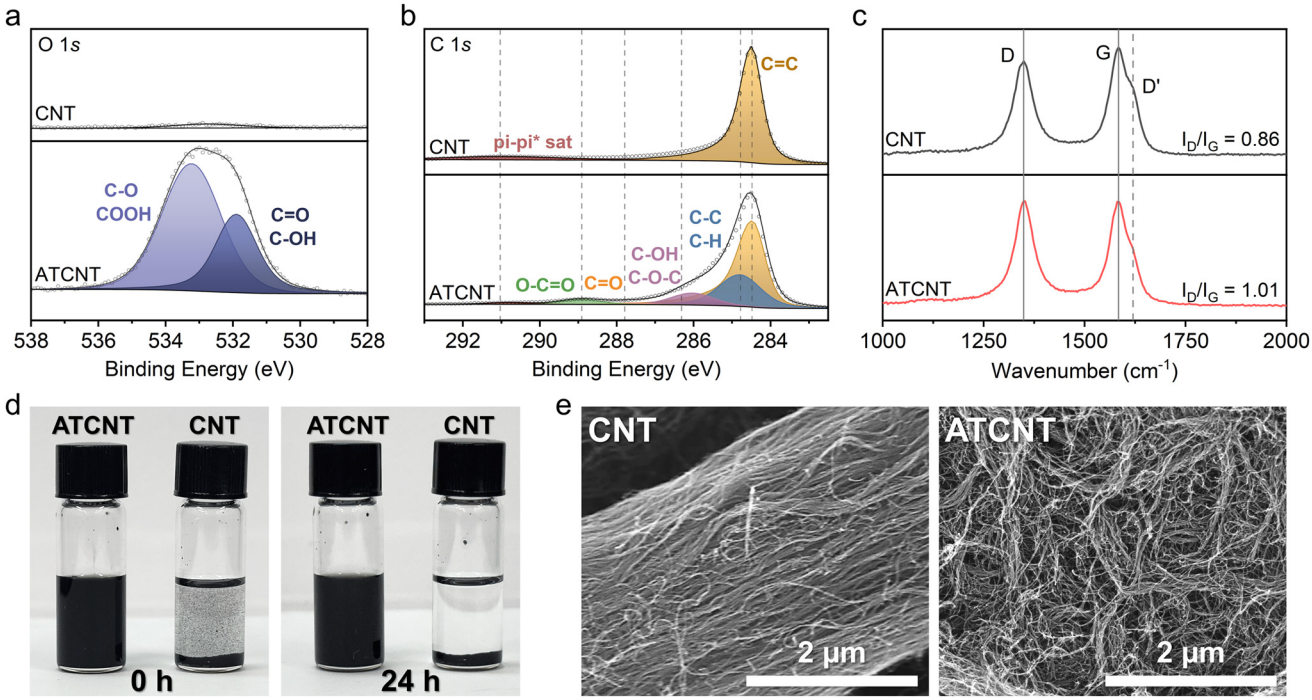

Fig. 4 Characterization of CNTs and ATCNTs. (a) O 1s and (b) C 1s XPS spectra of CNTs/ATCNTs. Due to the highly graphitic nature of CNTs, the spectra were charge corrected to C 1s C═C at 284.5 eV. (c) Raman spectra of CNTs/ATCNTs. (d) Images of 1 wt% CNTs/ATCNTs suspended in NMP *via* bath sonication immediately after (0 h) and 24 h later. (e) SEM images of CNTs and ATCNTs.

with EDS mapping. Two DS electrode compositions were prepared, each containing 90 wt% LMNO, 5 wt% PVDF, and 5 wt% of CNTs/ATCNTs designated as DS-CNT and DS-ATCNT respectively. For comparison, a ball-milled CNT electrode with the same 90 : 5 : 5 ratio (BM-CNT) was also prepared. Complete procedural details regarding slurry and electrode preparation are outlined in the Methods section.

Cross-sectional SEM-EDS analysis (Fig. 5a–c) illustrates the differences in carbon distribution across these three electrode compositions. In these maps, LMNO is represented in blue, carbon and PVDF in red, and electrode porosity in white. The DS-CNT electrode (Fig. 5a) exhibits poor carbon dispersion, with large and uneven CNT aggregates and micrometer-scale porosity that exceeds what is required for effective electrolyte wetting and instead disrupts electronic contact and percolation within the electrode. Enlarged pores and poor carbon dispersion and percolation have previously been shown to limit capacity and accelerate capacity degradation.[7] Conversely, DS-ATCNT (Fig. 5b) demonstrates improved carbon homogeneity, characterized by uniform distribution and minimal porosity. This uniform network maximizes electronic connectivity and is expected to markedly enhance electrochemical performance. Finally, the BM-CNT electrode (Fig. 5c) exhibits the best carbon distribution relative to DS-ATCNT and DS-CNT.

These observations demonstrate that the DS method, utilizing ATCNTs, simultaneously achieves effective enough carbon dispersion and percolation without requiring mechanical carbon milling. Consequently, the use of functionalized CNTs to facilitate DS film preparation, compared to additional mechanical carbon mixing steps, offers a practical solution that aligns closely with established electrode processing methodologies, providing a pathway toward industrially viable DRX cathode preparation.

XPS analysis was performed on BM-CNT and DS-ATCNT electrodes. Because surface oxidation during wet-electrode fabrication in air could obscure the intrinsic CTR-induced changes, the electrode surfaces were lightly etched with Ar ions prior to measurement to remove putative oxidized surface layers formed after air exposure. The O 1s spectra (Fig. 5d) reveal a stronger carbonate peak at ~532.2 eV in the BM-CNT film, consistent with more extensive CTR, whereas the DS-ATCNT electrode shows an enhanced peak at ~533.5 eV, attributed to oxidative functional groups introduced during acid treatment, in line with the C–O/COOH feature observed in Fig. 4a. The C 1s spectra (Fig. S9) further support this trend, displaying a more pronounced CO_3^{2-} peak at ~290.3 eV in the BM-CNT electrode, again pointing to a higher degree of CTR. Finally, the Mn 3s spectra (Fig. 5e) provide direct evidence of Mn reduction from CTR in the BM-CNT film, with an energy separation of 5.97 eV compared to only 5.47 eV for the DS-ATCNT film. Collectively, these results confirm that DS-ATCNT electrode preparation effectively mitigates CTR.

Finally, the electrochemical performance of the electrode films was evaluated with Li||LMNO half-cells (90 : 5 : 5, LMNO : CNT/ATCNT/CB : PVDF, 1.5–4.8 V, 40 mA g^{-1}, 25 °C), with all LMNO electrodes prepared by slurry casting in air. Key

© 2026 The Author(s). Published by the Royal Society of Chemistry

Open Access Article. Published on 16 February 2026. Downloaded on 5/8/2026 1:45:22 AM.
This article is licensed under a Creative Commons Attribution 3.0 Unported Licence.

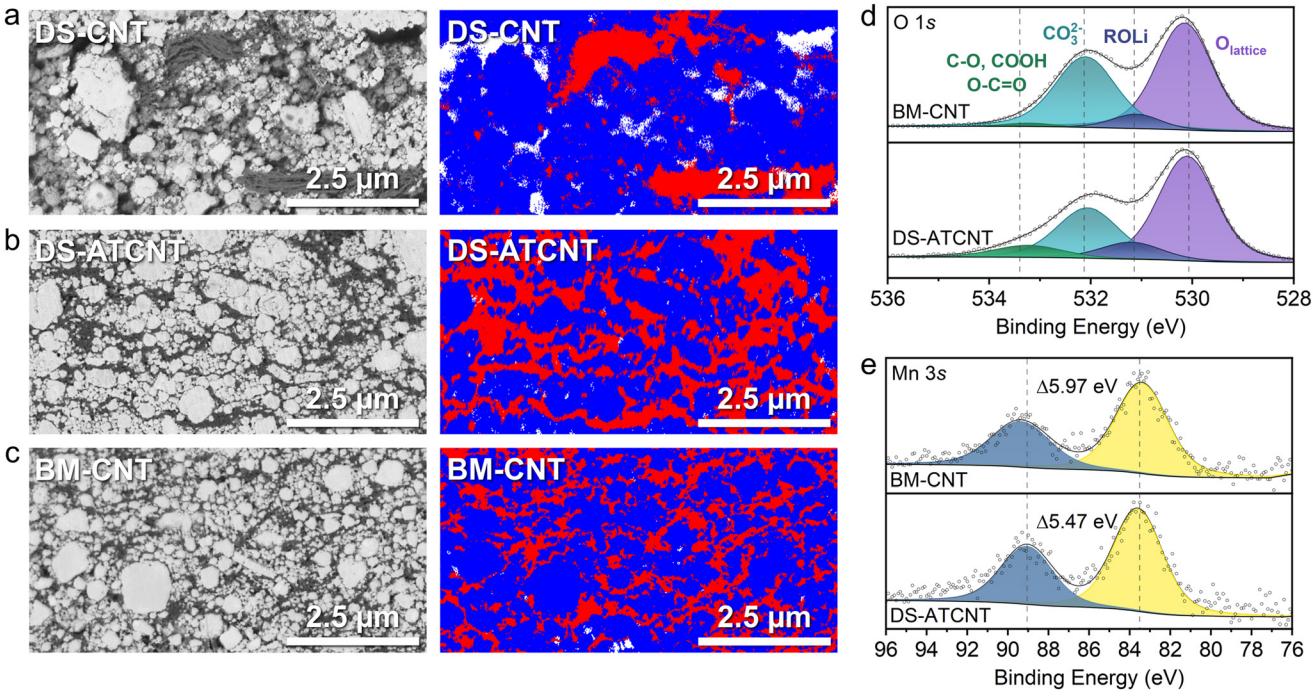

Fig. 5 Characterization of LMNO electrodes with different carbon sources and processing conditions. Cross-sectional SEM images and corresponding EDS maps of pristine 90 : 5 : 5 electrodes (a) DS-CNT, (b) DS-ATCNT and (c) BM-CNT, where red, blue and white are represented by carbon/PVDF, LMNO, and porosity, respectively. (d) O 1s and (e) Mn 3s XPS spectra of BM-CNT and DS-ATCNT films charge corrected to C 1s C=C at 284.5 eV.

electrode-level parameters, including electrode density, porosity, and areal loading, for representative electrodes, are summarized in Fig. S10. Fig. 6a compares the first-cycle voltage profiles of the different methods used. Clear differences are observed depending on the carbon type, its dispersion, and the processing approach. The poorly carbon-dispersed DS-CNT electrode delivers only 131 mAh g^{-1} in discharge capacity, whereas DS-ATCNT shows an impressive 274 mAh g^{-1} discharge capacity. BM-CNT attains a comparable initial charge capacity to DS-ATCNT but only a 246 mAh g^{-1} discharge capacity. Even with the improved dispersion of CNTs in the BM-CNT electrode, the increased surface carbonate species formed during CTR hinders electrical conductivity and reduces its absolute capacity. The OCV during the resting stage before cycling is also lower for BM-CNT (2.572 V) than for DS-ATCNT (2.838 V), consistent with a more reduced starting state from CTR (supported by Mn 3s XPS in Fig. 5e), although air exposure during the wet-electrode process (which makes CTR-damaged samples prone to re-oxidation and thus gives a higher OCV) likely renders the value less intrinsic to the degree of CTR than when LMNO electrodes are fabricated as dry electrodes in a glovebox.

An attempt to cycle a BM-CB wet-cast electrode with the same 90 : 5 : 5 composition yielded negligible capacity (Fig. 6a), similar to our prior observations with $Li_{1.2}Mn_{0.4}Ti_{0.4}O_2$ (LMTO).[7] In contrast, when a DS-CB 90 : 5 : 5 electrode is used, LMNO delivers a notable capacity of ~200 mAh g^{-1} in the first discharge, although smaller than that of the DS-ATCNT or BM-CNT electrodes, even with only 5 wt% CB in the composite electrode. Since the 90(LMTO) : 5 (CB) : 5(PVDF) electrode in our previous study also employed mechanical CB mixing, we hypothesize that the negligible capacity observed for LMTO in that case (as with the BM-CB electrode here) was largely due to extensive CTR, which converted a significant portion of CB into insulating lithium-based surface species such as Li_2CO_3. With only 5 wt% CB initially, the residual conductive carbon after CTR was likely insufficient to enable electrical percolation within the electrode matrix, especially given CBs relatively small specific surface area compared to CNTs. Interestingly, the DS-CB electrode even outperforms the DS-CNT electrode, despite CNTs being superior conductors with a higher specific surface area. This counterintuitive result is attributed to the extremely poor dispersion of CNTs in NMP, which leads to a less uniform distribution in the composite electrode compared to CB, which disperses far more readily.

Fig. 6b compares the discharge capacity of LMNO in DS-ATCNT, BM-CNT, and DS-CNT electrodes over 50 cycles (see Fig. S11 for both charge/discharge capacity and coulombic efficiency). Among them, DS-CNT exhibits the lowest discharge capacity (<100 mAh g^{-1}) and the poorest retention, with 55.7% remaining after 50 cycles. In contrast, DS-ATCNT delivers the highest capacity and achieves an improved capacity retention of 67.2%. Its retention is slightly lower than that of BM-CNT (69.1%), mainly because the ~25 mAh g^{-1} smaller initial capacity of BM-CNT compared with DS-ATCNT results in a

© 2026 The Author(s). Published by the Royal Society of Chemistry

Open Access Article. Published on 16 February 2026. Downloaded on 5/8/2026 1:45:22 AM.
This article is licensed under a Creative Commons Attribution 3.0 Unported Licence.

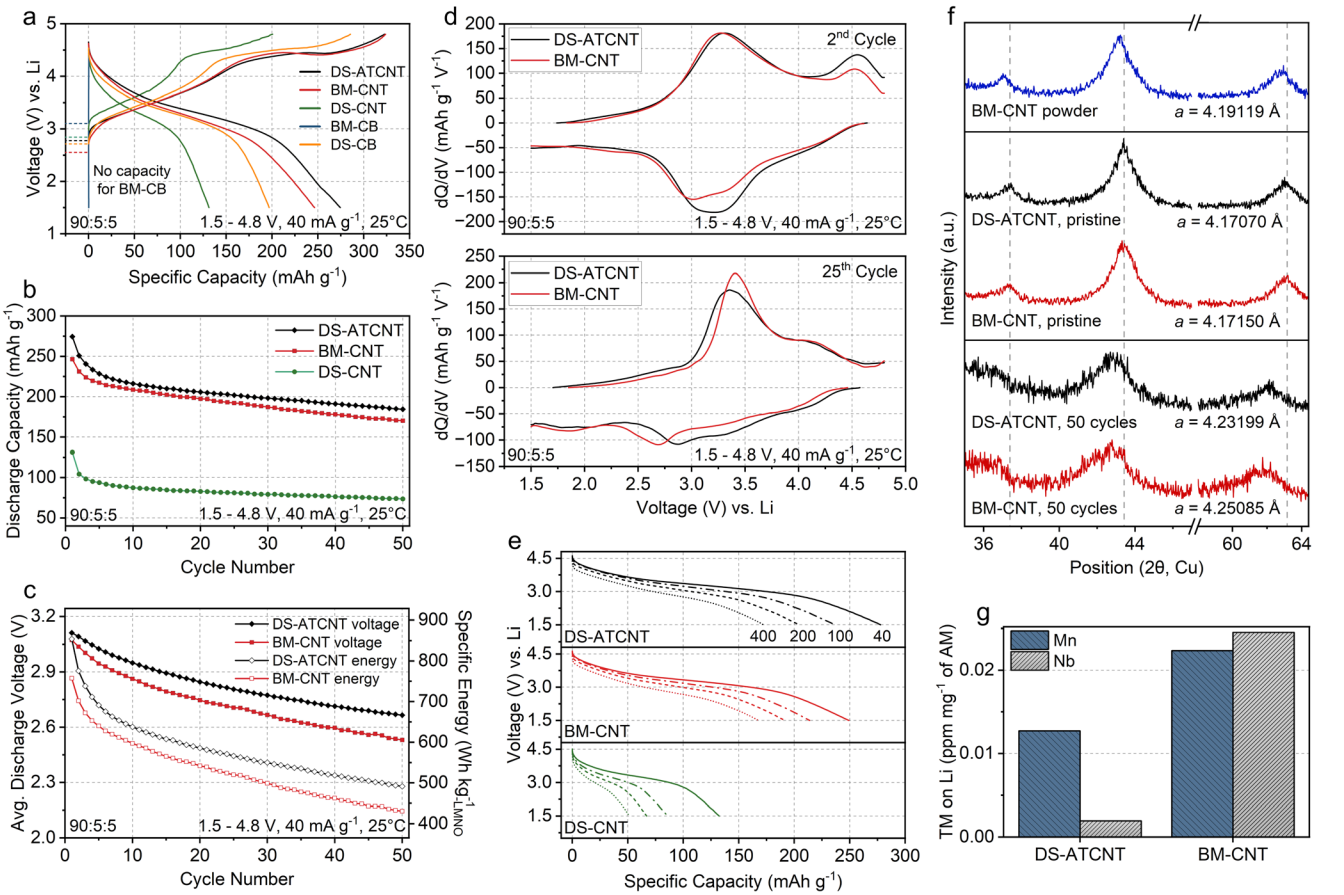

Fig. 6 Electrochemical performance and post-cycling analysis of LMNO electrodes with different carbon sources and processing conditions. (a) 1st-Cycle voltage profiles of LMNO; DS-ATCNT, BM-CNT, DS-CNT, BM-CB and DS-CB cycled at 40 mA g^{-1} between 1.5–4.8 V. (b) Discharge capacity retention of DS-ATCNT, BM-CNT and DS-CNT cells over 50 cycles. (c) Average discharge voltage and specific energy of DS-ATCNT and BM-CNT cells over 50 cycles. (d) dQ/dV of the 2nd and 25th cycle of the DS-ATCNT and BM-CNT cells. (e) Rate capability of DS-ATCNT, BM-CNT and DS-CNT. Discharge rates used are 40, 100, 200 and 400 mA g^{-1}. (f) XRD of BM-CNT powder and pristine/50 cycles BM-CNT/DS-ATCNT electrodes. (g) Concentration of Mn and Nb detected on Li-metal anode after 50 cycles, determined by ICP-OES for DS-ATCNT and BM-CNT cells.

smaller denominator in the retention calculation. Notably, the DS-ATCNT electrode exhibits a higher average discharge voltage than the BM-CNT electrode (Fig. 6c), which is reasonable given the circumvention of CTR in DS-ATCNT. By combining higher capacity with higher operating voltage, DS-ATCNT consistently delivers greater specific discharge energy than BM-CNT, although further optimization of BM-CNT may help minimize CTR during electrode preparation and improve its performance.

dQ/dV analysis of the second-cycle voltage profiles of DS-ATCNT and BM-CNT cells (Fig. 6d) reveals a stronger oxygen oxidation peak at ~4.5 V during charge in DS-ATCNT compared with BM-CNT cells. DS-ATCNT also exhibits a reduction peak at ~3.2 V, slightly higher than the ~3.0–3.2 V peak observed in BM-CNT. By the 25th cycle, the charge and discharge peaks become less distinct and broaden in both cells, likely due to O-redox-related side reactions of LMNO, which promote oxygen loss and cathode–electrolyte interphase (CEI) layer formation. Nevertheless, DS-ATCNT cells consistently display discharge dQ/dV peaks at higher voltages, indicating that higher-voltage redox processes remain more prominent in DS-ATCNT than in BM-CNT even after extended cycling.

We performed rate capability tests on the DS-ATCNT, BM-CNT, and DS-CNT electrodes by charging them to 4.8 V at 40 mA g^{-1} and then discharging at 40, 100, 200, and 400 mA g^{-1} down to 1.5 V (Fig. 6e). The DS-ATCNT electrode delivers ~277 mAh g^{-1} at 40 mA g^{-1}, which decreases to ~236, ~205, and ~173 mAh g^{-1} as the discharge rate increases to 100, 200, and 400 mA g^{-1}, respectively. In comparison, BM-CNT delivers ~249, ~214, ~191, and ~168 mAh g^{-1}, while DS-CNT shows much lower values of ~132, ~86, ~67, and ~50 mAh g^{-1}. Thus, at every tested rate, the DS-ATCNT electrode exhibits higher capacity than both BM-CNT and DS-CNT.

Finally, we conducted post-cycling analysis of the DS-ATCNT and BM-CNT cells on both the cathode and the Li-metal anode. Fig. 6f presents the XRD patterns and lattice parameters obtained by Rietveld refinement of the BM-CNT and DS-ATCNT cathodes before cycling (pristine) and after 50 cycles, along with the XRD data of the powder used to prepare

© 2026 The Author(s). Published by the Royal Society of Chemistry

Open Access Article. Published on 16 February 2026. Downloaded on 5/8/2026 1:45:22 AM. This article is licensed under a Creative Commons Attribution 3.0 Unported Licence.

the BM-CNT electrode (full refinement details in Fig. S12). Both pristine electrodes exhibit similar LMNO lattice parameters of 4.17070 Å (DS-ATCNT) and 4.17150 Å (BM-CNT). After 50 cycles, these values increase to 4.23199 Å for DS-ATCNT and 4.25085 Å for BM-CNT. Such irreversible lattice expansion in DRX materials is typically linked to the introduction of reduced TM species (*e.g.*, Mn^{2+}, which is larger than Mn^{3+}), together with oxygen vacancy injection arising from oxygen loss, which reduces electrostatic screening and enhances cation–cation repulsion. The larger lattice expansion observed in the BM-CNT electrode therefore suggests more severe structural damage associated with oxygen loss. Additionally, BM-CNT exhibits a greater degree of XRD peak broadening after cycling, indicating more extensive amorphization of LMNO.

Fig. 6g further presents the elemental analysis of the Li-metal anodes after 50 cycles. While both Mn and Nb are detected, the Li anode paired with the DS-ATCNT electrode contains approximately 43% less Mn and only a negligible amount of Nb compared with the BM-CNT case, indicating a more stable LMNO surface chemistry in the DS-ATCNT electrode. Notably, the amount of Nb detected on the Li anode in the BM-CNT cell (~0.028 ppm mg^{-1} of LMNO) is comparable to that measured for the 70 : 20(CB) : 10 half-cells with varying mechanical CB mixing (~0.035 ppm mg^{-1} of LMNO, Fig. 3h), whereas the Nb level for the DS-ATCNT cell is only ~0.002 ppm mg^{-1} of LMNO. This result shows that Nb dissolution, which appears relatively insensitive to the extent of CTR under mechanical carbon mixing, can nevertheless be strongly suppressed when the ball-milling step is avoided, most likely by limiting the formation of under-coordinated Nb^{5+} environments at the DRX particle surface.

Together, these results show that LMNO in the DS-ATCNT electrode experiences less structural and interfacial degradation during cycling, which underpins its superior capacity, operating voltage, and capacity retention compared with the BM-CNT electrode. Moreover, the evolution of the average charge and discharge voltages and the electrochemical impedance spectroscopy (EIS) results show that the DS-ATCNT approach yields lower apparent interfacial and charge-transfer resistance both before and after cycling (Fig. S13), indicating improved interfacial stability at the cell level. The reduced impedance lowers the discharge overpotential, while the suppression of CTR preserves a higher thermodynamic electrode potential, together resulting in a higher average discharge voltage.

It is important to note that although the voltage, capacity, and rate capability advantages of the DS-ATCNT electrode were demonstrated here, the extent of these benefits is expected to depend on the DRX composition, cycling conditions, and the paired electrolyte, as all of these factors can influence oxygen loss from the DRX lattice and the resulting interfacial stability during prolonged cycling. While avoiding CTR-induced oxygen loss or surface carbonate formation during electrode fabrication enables a higher operating voltage and capacity for the DS-ATCNT electrode, oxygen loss induced during electrochemical cycling, which can be significant under high-voltage operation in conventional carbonate electrolytes, can electrochemically reduce the DRX active material and generate insulating surface carbonate species. These processes may progressively mask the initial advantages upon extended cycling.

Moreover, although the electrochemical evaluation in this work is performed in Li-metal half-cells, the degradation mechanisms associated with CTR are expected to be directly relevant to full-cell configurations. In particular, CTR at the cathode can promote transition-metal dissolution, which is widely recognized as a key contributor to full-cell degradation through cathode–anode cross-talk. The dissolved metal species can migrate to the anode, where they destabilize the solid–electrolyte interphase and catalyze electrolyte decomposition, processes that are not captured in half-cell measurements. In addition, CTR-induced degradation of the electronic percolation network in the cathode is expected to contribute to impedance growth in both half-cells and full-cells. Consequently, suppressing CTR during electrode processing is anticipated to improve full-cell performance by mitigating impedance growth, reducing transition-metal cross-talk, and enhancing coulombic efficiency.

Outlook on DRX electrode process engineering

Our identification of mechanically induced CTR and its suppression through the DS-ATCNT method highlights the critical role of carbon mixing protocols in preparing Mn-DRX cathodes.

Although this work focuses on a single Mn-DRX composition, CTR during mechanical carbon mixing or coating is expected to be broadly relevant to a wide range of Mn-DRX systems, with its severity governed by the Mn oxidation state and the redox energetics of the as-synthesized materials. Most reported Mn-DRX cathodes are Mn^{3+}-based and commonly incorporate high-valent cations such as Nb^{5+} or Ti^{4+}. In these materials, Mn^{3+} can be readily reduced to Mn^{2+}, rendering them intrinsically susceptible to CTR during mechanical carbon mixing. Moreover, Mn-DRX compounds exhibiting partial spinel-like cation ordering, such as $Li_{1.68}Mn_{1.6}O_{3.7}F_{0.3}$, are often reported to contain mixed Mn^{3+}/Mn^{4+} species in the as-synthesized state. The presence of higher-valent Mn^{4+} lowers the electronic chemical potential of the lattice and is therefore expected to further promote CTR-induced reduction under mechanical carbon mixing conditions. In contrast, Mn^{2+}-based DRX systems, including fluorinated Mn^{2+}–Nb^{5+} or Mn^{2+}–Ti^{4+} compositions, are expected to be more resistant to CTR, because further reduction of Mn^{2+} or of the accompanying high-valent cations is thermodynamically less favorable.

Inadequate control of mechanical mixing can damage DRX particles, complicating efforts to evaluate or design new DRX compositions with improved performance. This issue is reflected in the literature, where reported performance metrics often vary widely, even for the same composition. For example, the voltage profiles of LMNO ($Li_{1.2}Mn_{0.6}Nb_{0.2}O_2$) reported by Lee *et al.*[17] and Kwon *et al.*[47] differ substantially: the latter shows a much less pronounced oxygen oxidation plateau on

Open Access Article. Published on 16 February 2026. Downloaded on 5/8/2026 1:45:22 AM. This article is licensed under a Creative Commons Attribution 3.0 Unported Licence.

charge, closely resembling the voltage profile of heavily CTR-damaged LMNO (*e.g.*, 500-1 CB mixed LMNO with ball milling, Fig. 3a) in this study. Notably, even the 300-1 CB ball-milled LMNO in the 70 : 20 : 10 electrode of Fig. 3a already exhibits a diminished oxygen oxidation plateau on the first charge compared with the DS-ATCNT 90 : 5 : 5 electrode in Fig. 6a, indicating that even relatively mild ball milling can significantly damage LMNO when combined with a high carbon content. By demonstrating how different ball milling conditions affect their capacity, specific energy, voltage profile, and retention, our work raises concerns about the reliability of previously reported values and underscores the need for standardized electrode preparation protocols to enable meaningful comparisons across the DRX research community.

In this regard, our demonstration of the direct electrode-slurry mixing method for achieving uniform carbon dispersion without ball milling provides valuable guidance for standardizing electrode preparation protocols, ensuring consistent and transferable results across the literature, and simplifying DRX electrode processing toward compatibility with scalable commercial NMC production. Direct slurry-based carbon mixing eliminates the mechanical mixing step in cathode fabrication, reducing production costs and improving the reproducibility of DRX cathode manufacturing; however, as with any electrode fabrication approach, the DS-ATCNT processing parameters must be adjusted when the batch size or the microstructural characteristics of the DRX particles change to maintain a uniform dispersion of active material, conductive carbon, and binder after slurry casting and drying. For example, solvent content, slurry viscosity, and mixing conditions should be optimized to ensure stable dispersion and homogeneous electrode formation, particularly when scaling to kilogram-scale batches.

The superior or at least comparable performance of our DS-ATCNT electrode relative to the BM-CNT electrode (often regarded as mechanically carbon-coated) questions the necessity of mechanical or chemical carbon coating to achieve high performance in Mn-DRX. Importantly, overcoming the poor electronic conductivity of DRX particles only requires establishing conductive pathways in intimate contact with the active particles, rather than enforcing carbon coatings. Both mechanical carbon coating or mixing of pre-pulverized DRX particles and one-step carbon coating during DRX particle pulverization leads to similar CTR-related damage (Fig. 3, S6 and S7), indicating that forcing carbon directly onto DRX particles, either mechanically or chemically, inevitably carries a risk of CTR. Although one-step carbon coating or mixing during particle pulverization involves the same number of pulverization steps as our DS-ATCNT approach and therefore appears similarly attractive from a processing standpoint,[48,49] it still exposes the DRX particles to CTR. In contrast, our direct electrode-slurry carbon mixing method avoids CTR while achieving a uniform carbon distribution, clearly demonstrating that homogeneous carbon dispersion within the composite DRX electrode, rather than direct carbon coating of individual particles, is the key requirement for high electrochemical performance.

While our demonstration of a DS-ATCNT electrode highlights the potential of direct electrode-slurry carbon mixing for DRX particles, more in-depth and systematic studies of carbon functionalization are warranted. In this work, acid treatment of CNTs was selected primarily for its simplicity; however, the functionalization process was not optimized to maximize electrode performance, nor was CNT selection based on a systematic evaluation of products with different dimensions or crystallinities that can affect their performance and conductivities.[7,50–52] Furthermore, the behavior of functional polar groups that enhance CNT dispersion in solvents remains unclear during cycling. If these groups undergo significant side reactions with the electrolyte, additional degradation pathways may emerge. Beyond CNT functionalization, it is also important to understand the fundamental adhesion properties between DRX particles which depend on surface termination, conductive carbon, and binders. Such understanding would enable a balanced interfacial preference that optimizes the spatial distribution of active DRX particles, carbon, and binder during electrode fabrication.

Overall, eliminating mechanical ball milling steps, whether with or without carbon, simplifies electrode preparation and reduces associated costs. In this study, small LMNO particles were prepared *via* solid-state synthesis followed by mechanical ball milling, reflecting the typical approach used in the literature to produce high-capacity DRX nanoparticles. However, we recently demonstrated that ball milling can be avoided through a modified molten-salt method, which yields highly crystalline DRX particles with sufficiently small particle sizes to achieve high capacities. This approach not only improves the intrinsic stability of the DRX particles but also promotes uniform particle distribution within the composite electrode.[53] In that previous work, however, we employed mechanical carbon mixing for carbon coating and dispersion, which could damage single-particle crystallinity and trigger CTR. The present study shows that even this carbon dispersion step can be achieved without ball milling, making the entire DRX electrode fabrication process simpler, more reproducible, and more cost-effective. Looking ahead, a deeper understanding of binder interactions with DRX particles will also be important for advancing electrode design. Taken together, this work establishes a blueprint for sustainable electrode-level engineering of DRX cathodes, paving the way for practical Ni- and Co-free LIBs.

Conclusions

In summary, this study found that mechanical carbon milling, often considered essential for Mn-DRX materials, had detrimental effects on their chemistry, structure, and electrochemical performance. For LMNO ($Li_{1.2}Mn_{0.6}Nb_{0.2}O_2$), stronger milling led to increased surface carbonate formation, Mn reduction, and irreversible lattice damage, which accelerated side reactions with the electrolyte and resulted in lower operating potentials, reduced capacity and retention (303 mAh g^{-1}

© 2026 The Author(s). Published by the Royal Society of Chemistry

Open Access Article. Published on 16 February 2026. Downloaded on 5/8/2026 1:45:22 AM. This article is licensed under a Creative Commons Attribution 3.0 Unported Licence.

and 54.2% at 300-1 *vs.* 242 mAh g^{-1} and 31.9% at 600-1 after 50 cycles), and higher overpotentials. These changes ultimately counteracted the intended benefits of carbon mixing and limited the achievable specific energy. By contrast, simple acid treatment of CNTs enabled direct electrode-slurry mixing without mechanical milling, which achieved uniform carbon dispersion and delivered higher capacity and operating voltage even at high active material loadings (274 mAh g^{-1} at 90 wt% AM). Overall, this work provided new insights into the impact of electrode processing and carbon selection on Mn-DRX and offered a practical strategy to simplify fabrication while maintaining strong electrochemical performance.

Methods

Material synthesis

Stoichiometric amounts of Mn_2O_3 and Nb_2O_5 were mixed with a 10% excess of Li_2CO_3 to compensate for lithium loss during calcination. A total of 10 g of the precursor mixture was milled using a planetary ball mill (Fritsch, PULVERISETTE 7 premium line) at 400 rpm for 6 h in 80 mL stainless-steel jars sealed inside an argon-filled glovebox. The milling media consisted of twenty 10 mm and forty 5 mm stainless-steel balls. After milling, the powders were collected in an argon-filled glovebox and subsequently calcined at 1050 °C for 2 h under argon flow in a tube furnace with a heating rate of 5 °C min^{-1}, followed by cooling to room temperature. Next, 1.5 g of the as-synthesized LMNO (AS-LMNO) was transferred into a 45 mL stainless-steel jar along with five 10 mm and ten 5 mm stainless-steel balls then subsequently pulverized in a planetary ball mill at 500 rpm for 5 h. The resulting as-pulverized LMNO (AP-LMNO) was then collected and stored in an argon-filled glovebox. For the one-step carbon coating experiments, 280 mg of AS-LMNO and 80 mg of Super C65 carbon black (CB, MSE Supplies) were added to a 45 mL stainless-steel jar with 20 g of 3 mm stainless-steel balls. Mixing was performed at either 300 rpm for 1 h, 600 rpm for 1 h or 600 rpm for 5 h in a planetary ball mill. The resulting CB mixed AS-LMNO powders were then collected and stored in an argon-filled glovebox before characterization.

To prepare acid-treated multiwall carbon nanotubes (ATCNTs), 300 mg of multi-walled carbon nanotubes (CNTs, Nano Solution, Korea) were dispersed in deionized water *via* probe sonication. A 2 : 1 mixture of 15.8 M HNO_3 (nitric acid, Sigma-Aldrich, 70%) and 18 M H_2SO_4 (sulfuric acid, Sigma-Aldrich, 95.0%–98.0%) was then added and stirred at 90 °C for 18 h. After cooling, the solution was diluted with deionized water and repeatedly washed by suction filtration until the filtrate reached a neutral pH. The resulting ATCNTs were then collected and freeze-dried for 24 h followed by further drying in a vacuum oven at 120 °C for 16 h.

Characterization

X-ray diffraction (XRD) was employed to evaluate the crystallinity and phase purity of the samples. Patterns were recorded on a Malvern PANalytical Empyrean diffractometer with Cu Kα radiation over a 2θ range of 10–90°. For post-cycling electrode analysis, coin cells were disassembled in an argon-filled glovebox and thoroughly rinsed with dimethyl carbonate (DMC) to remove residual electrolyte prior to analysis. Electrodes were sealed in an airtight holder under argon with a polyether ether ketone (PEEK) domed lid and Si (510) zero-background insert (Anton Paar). All Rietveld refinement was performed using PANalytical X'Pert HighScore Plus software.

The morphology of AS-LMNO, AP-LMNO, CNTs, and ATCNTs was observed using a Hitachi SU8000 scanning electron microscope (SEM). Cross-sections of the electrode films were prepared with a Hitachi IM4000Plus Ar-ion milling system operating at 6 keV. To understand the elemental distribution in the electrode film cross-sections and carbon-mixed LMNO samples, SEM images and energy dispersive X-ray spectroscopy (EDS) analysis was performed using a Hitachi SU9000 Field Emission-SEM/STEM with a HABSE detector at an accelerating voltage of 1.2 kV. EDS mapping was conducted using an Oxford Instruments Extreme detector. Transmission electron microscopy (TEM) images of the 300 rpm-1 h and 600 rpm-1 h CB mixed powders were acquired using a Thermo-Scientific Talos F200X G2 STEM operated at 200 kV. To quantify electrode parameters (areal loading, thickness, bulk density, active material density, and porosity), DS-ATCNT, BM-CNT, and BM-CB electrodes were cut using a precision die. Cross-sectional images were acquired using a Hitachi SU3500 variable-pressure SEM, and the above parameters were determined from the measured cross-sectional thickness and electrode mass/area.

X-ray Photoelectron Spectroscopy (XPS) was performed on a Thermos Fisher-Scientific Nexsa G2 with Al Kα radiation as the X-ray source. All samples were prepared in an argon-filled glovebox and then transferred into the instrument using an airtight holder to prevent air exposure. XPS spectra were recorded with a 400 μm spot size at a constant pass energy. Data analysis was carried out using Thermo-Scientific Avantage software. For the CB mixed samples, charge correction was performed using the C 1s C–C/C–H peak at 284.8 eV. For the CNT, ATCNT, and BM-CNT electrodes, charge correction was performed using the C 1s C=C peak at 284.5 eV. For the wet-processed electrodes that are exposed to air during fabrication, argon-ion etching was used to clean the surface before analysis. Raman measurements were performed on a Thermo Fisher-Scientific DXR3 Raman Microscope with a 532 nm excitation laser.

To conduct elemental analysis, inductively coupled plasma optical emission spectroscopy (ICP-OES) was carried out using a Thermo-Scientific iCAP 6000. Calibration standards were prepared by diluting Mn (1003 ± 5 mg L^{-1}) and Nb (1001 ± 3 mg L^{-1}) stock solutions (in 2 wt% HNO_3, TraceCERT®, Sigma-Aldrich). The coin cells were disassembled in an argon-filled glovebox, and the lithium metal anode thoroughly rinsed with DMC to remove residual electrolyte. The lithium metal anode was then removed from the glovebox and dissolved in a 2 wt% HNO_3 solution before analysis.

© 2026 The Author(s). Published by the Royal Society of Chemistry

Open Access Article. Published on 16 February 2026. Downloaded on 5/8/2026 1:45:22 AM.
This article is licensed under a Creative Commons Attribution 3.0 Unported Licence.

Electrochemical characterization

For the preparation of cathode films, two different methods were employed. Dry-processed films: 280 mg of AP-LMNO and 80 mg of Super C65 carbon black (CB, MSE Supplies) were added to 45 mL stainless-steel jars with 20 g of 3 mm stainless-steel balls, sealed in an argon-filled glovebox and then milled using a planetary ball mill at 300 rpm for 1 h. Remaining samples were prepared the same way but with different rotation speeds (400, 500, or 600 rpm) and/or mixing times (1 or 5 h). Next, 90 mg of the CB mixed powder was mixed with 10 mg of polytetrafluoroethylene binder (PTFE, Sigma-Aldrich) using a mortar and pestle. The mixture was then rolled into thin films in an argon-filled glovebox and punched into 8 mm discs. The electrode composition was 70 wt% AP-LMNO, 20 wt% CB, and 10 wt% PTFE (70 : 20 : 10). Wet-processed (or direct electrode-slurry, DS) films: AP-LMNO was mixed with a conductive additive (ATCNTs, CNTs, or CB) with 5 wt% polyvinylidene fluoride binder (PVDF, MTI HSV900) dissolved in *N*-methylpyrrolidone (NMP, Sigma-Aldrich, 99.5%), plus additional NMP. Mixing was carried out in a Thinky mixer for 20 min. The slurry was then blade-cast (400 μm) onto aluminum foil (MSE Supplies, 99.5%, 15 μm) and dried under vacuum at 80 °C for 12 h. Electrodes were then calendared, punched into 13 mm discs, and further dried at 80 °C for 16 h under vacuum. The electrode composition was 90 wt% AP-LMNO, 5 wt% conductive additive, and 5 wt% PVDF (90 : 5 : 5). Reference BM-CNT electrodes were obtained by ball milling AP-LMNO and CNTs in a 45 mL stainless-steel jar sealed in an argon-filled glovebox with five 10 mm and ten 5 mm stainless-steel balls at 300 rpm for 30 min. The powder was then collected and processed with the same direct electrode-slurry procedure. The target active material loading for all wet-processed films was ~4 mg cm^{-2}.

Coin cells (CR2032, 316 stainless-steel) were assembled in an argon-filled glovebox with the composite films as the positive electrode and a lithium metal chip as the negative electrode (MSE Supplies, 15.6 mm diameter, 0.25 mm thick, 99.9%). A polypropylene separator (Celgard 3501) was used to prevent the contact of the positive and negative electrodes. 1 M $LiPF_6$ dissolved in ethylene carbonate and dimethyl carbonate (EC/DMC, 1 : 1 v/v) was used as the electrolyte. Galvanostatic charge/discharge and rate-capability tests were carried out using a Landt CT3002A battery testing system inside a temperature-controlled chamber (Landt LBI-300HT) at 25 °C. The specific capacity was calculated based on the mass of the active material (LMNO) in the cathode film. The data presented in the manuscript corresponds to the median-performing cell in terms of capacity and retention, selected to minimize bias and reflect typical behavior. Galvanostatic intermittent titration technique (GITT) was performed using a 3 h relaxation step after every charging/discharging increment of 5 mAh g^{-1} at a 20 mA g^{-1} rate. The Li diffusivity was calculated using the formula: $D_{Li} = [4/\pi\tau][(R_S/3)^2][((\Delta V_s)/(\Delta V_t))^2]$ and EC Box software.[54] The electrochemistry model leading to this formula assumes spherical electrode particles (radius: R_S) and $D_{Li}\tau \ll L_s^2$, where τ is the time duration of the pulse (900 s in the case of our test), and L_S is the characteristic dimension of the solid-phase material.[54] ΔV_s is the steady-state voltage change due to the current pulse and ΔV_t is the voltage change during the constant current pulse after subtracting the IR drop. We assume R_S = 100 nm because AP-LMNO typically has a secondary particle diameter of 200 nm ($d = 2R_S$). Electrochemical impedance spectroscopy (EIS) was performed on DS-ATCNT and BM-CNT Li-metal half-cells using a Biologic SP-200 potentiostat. Assembled half-cells were rested at open-circuit voltage for 12 h followed by an EIS measurement, after which galvanostatic cycling was started immediately. After 6 cycles (1.5–4.8 V, 40 mA g^{-1}) the cells were taken off the cycler and EIS measurements were performed at open-circuit voltage. Impedance spectra were collected with a 5 mV AC amplitude over 200 kHz to 5 mHz. Data are presented as Nyquist plots and fitting was performed using ZView2.

Author contributions

G. L., Y. Z., and J. L. planned the project. J. L. supervised all aspects of the research. G. L. and Y. Z. performed the overall experimental work along with the interpretation of the results. P. T. L., N. B., and R. G. performed SEM and assisted with its interpretation and analysis. G. L. and J. L. wrote the manuscript.

Conflicts of interest

There are no conflicts of interest to declare.

Data availability

All data supporting this study are included in the article and its supplementary information (SI). Supplementary information: additional figures and tables. See DOI: https://doi.org/10.1039/d5eb00236b.

Methods are described in the article. Further information is available from the corresponding author.

Acknowledgements

J. L. acknowledges funding support from Wildcat Discovery Technologies, Inc. and the NSERC Discovery Grant (RGPIN-2020-04463). R. G. acknowledges support from the NSERC Discovery Grant (RGPIN-2024-04977) and McGill Materials Characterization (MMC) at McGill University. G. L., Y. Z., and P. T. L. acknowledge support from the Vadasz Scholar Program, the McGill Engineering International Doctoral Award, and the Hatch Fellowship at McGill University, respectively.

© 2026 The Author(s). Published by the Royal Society of Chemistry

Open Access Article. Published on 16 February 2026. Downloaded on 5/8/2026 1:45:22 AM. This article is licensed under a Creative Commons Attribution 3.0 Unported Licence.

References

1 F. Degen, M. Winter, D. Bendig and J. Tübke, *Nat. Energy*, 2023, **8**, 1284–1295.
2 M. M. Li, J. M. Weller, D. M. Reed, V. L. Sprenkle and G. Li, *Joule*, 2023, **7**, 619–623.
3 A. A. Savina and A. M. Abakumov, *Heliyon*, 2023, **9**, e21881.
4 W.-J. Zhang, *J. Power Sources*, 2011, **196**, 2962–2970.
5 H. Li, R. Fong, M. Woo, H. Ahmed, D.-H. Seo, R. Malik and J. Lee, *Joule*, 2022, **6**, 53–91.
6 F. Liu, J. He, H. Chen, W. Yang, R. Yu and Z. Lun, *Adv. Funct. Mater.*, 2025, **35**, 2419907.
7 E. Lee, D.-H. Lee, S. Bessette, S.-W. Park, N. Brodusch, G. Lazaris, H. Kim, R. Malik, R. Gauvin and D.-H. Seo, *Energy Environ. Sci.*, 2024, **17**, 3753–3764.
8 B. Kang, J. Park, B. Kim, S.-O. Park, J. Yoo, S. Yu, H.-J. Kim, J.-H. Song and K. Kang, *Energy Environ. Sci.*, 2025, **18**, 2330–2341.
9 S. Patil, K. P. Koirala, M. J. Crafton, G. Yang, W. Y. Tsai, B. D. McCloskey, C. Wang, J. Nanda and E. C. Self, *ACS Appl. Mater. Interfaces*, 2023, **15**, 39253–39264.
10 Y. Wang, W. Choe, Y. Ding, R. Liu, D. Nordlund and D. Chen, *J. Am. Chem. Soc.*, 2025, **147**, 13437–13446.
11 H. Lee, M. Kim, H. Park, Y. Yoo, S. Na, H.-D. Lim, J. Kim and W.-S. Yoon, *Adv. Funct. Mater.*, 2024, **34**, 2312401.
12 V. C. Wu, E. A. Lawrence, T. Li, E. N. Bassey, C.-Y. Chang, B. J. Hwang, P.-E. Cabelguen and R. J. Clément, *Energy Environ. Sci.*, 2025, **18**, 8918–8928.
13 F. Duffner, N. Kronemeyer, J. Tübke, J. Leker, M. Winter and R. Schmuch, *Nat. Energy*, 2021, **6**, 123–134.
14 F. Duffner, L. Mauler, M. Wentker, J. Leker and M. Winter, *Int. J. Prod. Econ.*, 2021, **232**, 107982.
15 A. Kwade, W. Haselrieder, R. Leithoff, A. Modlinger, F. Dietrich and K. Droeder, *Nat. Energy*, 2018, **3**, 290–300.
16 S. Lee, S. Kang, Y. Choi, J. Kim, J. Yang, D. Han, K.-W. Nam, O. J. Borkiewicz, J. Zhang and Y.-M. Kang, *J. Am. Chem. Soc.*, 2024, **146**, 33845–33856.
17 J. Lee, C. Wang, R. Malik, Y. Dong, Y. Huang, D.-H. Seo and J. Li, *Adv. Energy Mater.*, 2021, **11**, 2100204.
18 R. Tatara, P. Karayaylali, Y. Yu, Y. Zhang, L. Giordano, F. Maglia, R. Jung, J. P. Schmidt, I. Lund and Y. Shao-Horn, *J. Electrochem. Soc.*, 2019, **166**, A5090.
19 E. Björklund, D. Brandell, M. Hahlin, K. Edström and R. Younesi, *J. Electrochem. Soc.*, 2017, **164**, A3054.
20 A. Guéguen, P. Novák and E. J. Berg, *J. Electrochem. Soc.*, 2016, **163**, A2545.
21 S. Malmgren, K. Ciosek, M. Hahlin, T. Gustafsson, M. Gorgoi, H. Rensmo and K. Edström, *Electrochim. Acta*, 2013, **97**, 23–32.
22 H. Chung, Z. Lebens-Higgins, B. Sayahpour, C. Mejia, A. Grenier, G. E. Kamm, Y. Li, R. Huang, L. F. J. Piper, K. W. Chapman, J.-M. Doux and Y. S. Meng, *J. Mater. Chem. A*, 2021, **9**, 1720–1732.
23 C.-T. Dinh, A. Jain, F. P. G. de Arquer, P. De Luna, J. Li, N. Wang, X. Zheng, J. Cai, B. Z. Gregory, O. Voznyy, B. Zhang, M. Liu, D. Sinton, E. J. Crumlin and E. H. Sargent, *Nat. Energy*, 2019, **4**, 107–114.
24 B. Laïk, M. Richet, N. Emery, S. Bach, L. Perrière, Y. Cotrebil, V. Russier, I. Guillot and P. Dubot, *ACS Omega*, 2024, **9**, 40707–40722.
25 W. Huang, C. Seok, L. Tao, C. Shi, J. Yao, D. Xia, A. T. Promi, K. Meyer, D. Yang, S. Liu, S. Hwang, D. Nordlund and F. Lin, *Adv. Energy Mater.*, 2025, **15**, 2501285.
26 Y.-C. Lu, E. J. Crumlin, G. M. Veith, J. R. Harding, E. Mutoro, L. Baggetto, N. J. Dudney, Z. Liu and Y. Shao-Horn, *Sci. Rep.*, 2012, **2**, 715.
27 N. Hornsveld, B. Put, W. M. M. Kessels, P. M. Vereecken and M. Creatore, *RSC Adv.*, 2017, **7**, 41359–41368.
28 Z. Zhou, X. Zheng, M. Liu, P. Liu, S. Han, Y. Chen, B. Lan, M. Sun and L. Yu, *ChemSusChem*, 2022, **15**, e202200612.
29 O. Y. Bisen, M. Baumung, M. Tatzel, C. A. Volkert and M. Risch, *Energy Adv.*, 2024, **3**, 504–514.
30 W. Guo, C. Dun, C. Yu, X. Song, F. Yang, W. Kuang, Y. Xie, S. Li, Z. Wang, J. Yu, G. Fu, J. Guo, M. A. Marcus, J. J. Urban, Q. Zhang and J. Qiu, *Nat. Commun.*, 2022, **13**, 1409.
31 E. S. Ilton, J. E. Post, P. J. Heaney, F. T. Ling and S. N. Kerisit, *Appl. Surf. Sci.*, 2016, **366**, 475–485.
32 G. C. Allen, S. J. Harris, J. A. Jutson and J. M. Dyke, *Appl. Surf. Sci.*, 1989, **37**, 111–134.
33 S. Ardizzone, C. L. Bianchi and D. Tirelli, *Colloids Surf., A*, 1998, **134**, 305–312.
34 V. Di Castro and G. Polzonetti, *J. Electron Spectrosc. Relat. Phenom.*, 1989, **48**, 117–123.
35 J. L. Junta and M. F. Hochella, *Geochim. Cosmochim. Acta*, 1994, **58**, 4985–4999.
36 Y. Wang, A. Outka, W. M. Takele, M. Avdeev, S. Sainio, R. Liu, V. Kee, W. Choe, B. Raji-Adefila, D. Nordlund, S. Zhou, W. H. Kan, T. G. Habteyes and D. Chen, *Adv. Mater.*, 2023, **35**, 2306396.
37 J. Lee, A. Urban, X. Li, D. Su, G. Hautier and G. Ceder, *Science*, 2014, **343**, 519–522.
38 D. Chen, W. H. Kan and G. Chen, *Adv. Energy Mater.*, 2019, **9**, 1901255.
39 C. Zhan, T. Wu, J. Lu and K. Amine, *Energy Environ. Sci.*, 2018, **11**, 243–257.
40 D. Xia, J. Yao, C. Shi, Q. Wang, C. Seok, A. Olayiwola, W. Huang, D. Nordlund, S. A. Chen, C.-J. Sun, L. Li, D. Hou, L. Quan, Y. Liu, H. Xiong and F. Lin, *Adv. Mater.*, 2025, **37**, 2501352.
41 H. Wang, A. Zhou, F. Peng, H. Yu and J. Yang, *J. Colloid Interface Sci.*, 2007, **316**, 277–283.
42 B. Smith, K. Wepasnick, K. E. Schrote, A. R. Bertele, W. P. Ball, C. O'Melia and D. H. Fairbrother, *Environ. Sci. Technol.*, 2009, **43**, 819–825.
43 C. S. Kam, T. L. Leung, F. Liu, A. B. Djurišić, M. H. Xie, W.-K. Chan, Y. Zhou and K. Shih, *RSC Adv.*, 2018, **8**, 18355–18362.
44 M. C. Biesinger, *Appl. Surf. Sci.*, 2022, **597**, 153681.
45 O. Beyssac, B. Goffé, J.-P. Petitet, E. Froigneux, M. Moreau and J.-N. Rouzaud, *Spectrochim. Acta, Part A*, 2003, **59**, 2267–2276.

© 2026 The Author(s). Published by the Royal Society of Chemistry

Open Access Article. Published on 16 February 2026. Downloaded on 5/8/2026 1:45:22 AM.
This article is licensed under a Creative Commons Attribution 3.0 Unported Licence.

46 S. A. Chernyak, A. S. Ivanov, K. I. Maslakov, A. V. Egorov, Z. Shen, S. S. Savilov and V. V. Lunin, *Phys. Chem. Chem. Phys.*, 2017, **19**, 2276–2285.
47 D.-H. Kwon, J. Lee, N. Artrith, H. Kim, L. Wu, Z. Lun, Y. Tian, Y. Zhu and G. Ceder, *Cell Rep. Phys. Sci.*, 2020, **1**, 100187.
48 J. Ahn, Y. Ha, R. Satish, R. Giovine, L. Li, J. Liu, C. Wang, R. J. Clement, R. Kostecki, W. Yang and G. Chen, *Adv. Energy Mater.*, 2022, **12**, 2200426.
49 D. Chen, J. Ahn, E. Self, J. Nanda and G. Chen, *J. Mater. Chem. A*, 2021, **9**, 7826–7837.
50 S. Patil, K. Koirala, M. Crafton, G. Yang, W.-Y. Tsai, B. McCloskey, C. Wang, J. Nanda and E. Self, *ACS Appl. Mater. Interfaces*, 2023, **15**, 39253–39264.
51 H.-M. Hau, T. Holstun, E. Lee, B. L. D. Rinkel, T. P. Mishra, M. Markuson DiPrince, R. S. Mohanakrishnan, E. C. Self, K. A. Persson, B. D. McCloskey and G. Ceder, *Adv. Mater.*, 2025, 2502766.
52 V. S. Avvaru, M. Zuba, B. L. Armstrong, S. Wang, D.-M. Kim, I. S. Buyuker, C. Siu, B. A. Helms, O. Kahvecioglu and H. Kim, *Electrochim. Acta*, 2025, **509**, 145302.
53 H. Ahmed, M. Woo, N. Dumaresq, P. Trevino Lara, R. Fong, S.-J. Lee, G. Lazaris, N. Mubarak, N. Brodusch, D.-H. Seo, R. Gauvin, G. P. Demopoulos and J. Lee, *Nat. Commun.*, 2025, **16**, 5806.
54 Z. Shen, L. Cao, C. D. Rahn and C.-Y. Wang, *J. Electrochem. Soc.*, 2013, **160**, A1842.

© 2026 The Author(s). Published by the Royal Society of Chemistry